FIRST IMAGES OF IMPULSIVE MILLIMETER EMISSION AND SPECTRAL ANALYSIS OF THE 1994 AUGUST 18 SOLAR FLARE

Adriana V. R. Silva* and Dale E. Gary
Solar Astronomy 264-33, Caltech, Pasadena, CA 91125

Stephen M. White
Dept. of Astronomy, University of Maryland, College Park, MD 20742

Robert P. Lin
Physics Department and Space Sciences Laboratory, University of California, Berkeley, CA 94720

Imke de Pater
Astronomy Department, University of California, Berkeley,CA 94720

Abstract. We present here the first images of impulsive millimeter emission of a flare. The flare on 1994 August 18 was simultaneously observed at millimeter (86 GHz), microwave (1-18 GHz), and soft and hard X–ray wavelengths. Images of millimeter, soft and hard X–ray emission show the same compact ($\lesssim 8''$) source. Both the impulsive and the gradual phases are studied in order to determine the emission mechanisms. During the impulsive phase, the radio spectrum was obtained by combining the millimeter with simultaneous microwave emission. Fitting the nonthermal radio spectra as gyrosynchrotron radiation from a model with constant magnetic field yield the physical properties of the flaring source, that is, total number of electrons, power–law index of the electron energy distribution, and the nonthermal source size. These results are then compared to those obtained from the hard X–ray spectra. The energy distribution of the energetic electrons inferred from the hard X–ray and radio spectra is found to follow a double power–law with slope $\sim$6-8 below 30-50 keV and $\sim$4 above those energies. The temporal evolution of the electron energy spectrum and its implication for the acceleration mechanism are then discussed. Comparison of millimeter and soft X–ray emissions during the gradual phase implies that the millimeter emission is free–free radiation from the same hot soft X–ray emitting plasma, and further suggests that the flare source contains multiple temperatures.

Key words: Sun: flares; Sun: radio radiation, Sun: X–rays

1. Introduction

The nonthermal millimeter emission in the impulsive phase of flares is believed to be produced by gyrosynchrotron radiation from electrons of $\gtrsim$ MeV energies (Ramaty 1969, Ramaty and Petrosian 1972, White and Kundu 1992). These are the same electrons that give rise to γ–ray continuum emission. Generally, however, only very large flares produce

* Physics Dept., New Jersey Institute of Technology, Newark, NJ 07102

γ–ray fluxes detectable by current instrumentation. The microwave emission is produced by electrons with a few hundred keV, whereas the usually observed hard X–rays originate from lower energy electrons ($\lesssim 100$ keV). Thus, a comparison of the emission at both radio and hard X–ray ($\lesssim 200$ keV) wavelengths provides information on the differential energy of the accelerated electrons from $\sim$20 keV up to MeV in energy.

Observations of some large flares (Frost and Dennis 1971, Smith and Orwig 1988, Dennis 1988) have shown that the hard X–ray spectra are best fit by double power–laws. These type of spectra may be evidence of two particle acceleration phases (Wild et al. 1963, de Jager 1969). In the two acceleration phases model, the first phase accelerates electrons up to energies of few hundred keV, perhaps by induced electric fields. The second phase occurs in a smaller fraction of flares and further accelerates electrons to relativistic electrons. Ions are also assumed to be accelerated up to tens of MeV during the second phase (Bai and Ramaty 1976). Fermi acceleration operating in a shock front is one of the suggested mechanisms for second phase acceleration. Comparison of hard X–ray and microwave emissions have also implied that the electron energy spectra is double power–law (Bai and Ramaty 1976, Kundu et al. 1994).

Since in most cases the temporal evolution of impulsive millimeter emission is observed to follow that of the impulsive microwave emission (Lim et al. 1992), both emissions are thought to be produced by the gyrosynchrotron mechanism. Then the radio spectrum from microwave to millimeter wavelengths can be used to determine the radio spectral slope. If the emission is optically thin, the slope of the radio spectrum is a direct measure of the power–law slope of the energy spectrum of the energetic electrons that produced the radio emission. Since most microwave observations only extend up to $\sim$15 GHz, the millimeter emission, which is clearly optically thin (Silva et al. 1996), is crucial in determining the high frequency radio index of flares that become optically thin only at frequencies $\gtrsim 10$ GHz.

Using the technique of interferometry, the quiet sun background and emission from extended sources are essentially eliminated, thus allowing the detection of millimeter emission of even small flares (e.g. B flares in the GOES classification). Kundu et al. (1990) were the first to report interferometric observations of flares at 86 GHz using the Berkeley–Illinois–Maryland Array (BIMA). Since at that time BIMA consisted of 3 elements, no imaging was possible. In 1994, BIMA was upgraded to 6 dishes, and the first millimeter images of a solar flare were reported (Silva et al. 1996). However, only the gradual thermal phase of the flare was studied since the interferometer was in a calibration scan at the time of the impulsive emission. Here we discuss images at millimeter wavelengths taken during both the impulsive and gradual phases of a flare on 1994 August 18. This flare was simultaneously detected at microwave frequencies and X–rays.

The temporal and spatial evolution of the flare at all wavelengths is described in Section 2. In section 3 we analyze the nonthermal radio spectrum, the differential energy distribution of accelerated electrons obtained through comparison of radio and hard X–ray spectra, and the results obtained from the millimeter maps and soft X–ray observations (during the gradual phase). The last section presents the discussion and conclusions.

2. Observations

The flare discussed in this paper peaked near 2046 UT on 18 August 1994, at heliographic location S11 W66 in active region AR7765. According to its GOES soft X–ray flux, the flare was classified as C3.5. The flare was simultaneously observed by Yohkoh's Soft (SXT, Tsuneta et al. 1991) and Hard (HXT, Kosugi et al. 1991) X–ray Telescopes (emission only in LO and M1–channels), in microwaves by the solar dedicated array at Owens Valley Radio Observatory (OVRO, Gary and Hurford 1990) in 45 frequencies from 1 to 18 GHz, and by BIMA at millimeter wavelengths (86 GHz). At the time of the observations, four BIMA antennas were operating, enabling us to image the millimeter source.

Unfortunately, due to non–optimum delay centers of the OVRO array, it is not possible to calibrate the correlated data from the three small dishes, and therefore map the microwave emission. The data from the two 27 m dishes, however, were not affected. Throughout this paper we will present the data from OVRO's baseline 12 (the correlated data of the two large antennas).

Figure 1 shows the time evolution of the X–ray and radio emissions. Because this is a small flare (C3.5), the count rates from HXT for this flare were low, with flux increases detected only in the LO and M1–channels. The hard X–ray emission, seen in Figure 1 (top panel), peaked at 2045:33 UT and lasted for about 2 minutes. The soft X–rays peaked at $\sim$2048 UT, and lasted for approximately 6 minutes. The microwave time profiles, plotted in the bottom panel of Figure 1, show a single rather broad peak shortly after 2046 UT. The 5 GHz emission (dotted line) peaks at 2046:03 UT, whereas the higher frequency emission, 14 GHz (dashed line), peaks at 2046:15. The microwave impulsive peak lasts for about one minute. Since the OVRO observation of this flare has only 12 s temporal resolution, it is not possible to determine the time delay exactly, though it is certain that the 14 GHz emission peaks later. The millimeter emission is also plotted in the bottom panel of Figure 1 (solid line); because its maximum flux density of ∼1.2 sfu is much less than that of the microwaves, we have plotted the 86 GHz flux density with a different scale, marked on the right hand side of the figure. Note that the BIMA emission peaks later than the microwave emission. Due to the uncertainty in the attenuation used to keep the strong solar signal from saturating the system, the absolute calibration for BIMA solar data is presently uncertain to within 50%.

The microwave and hard X–ray emissions start to rise simultaneously at 2045 UT. The low frequency microwaves (e.g. 5 GHz), however peak approximately 30 seconds after the main hard X–ray peak, whereas the high frequency emission (14 GHz) is further delayed by ∼12 seconds. Note, however, that there is still prominent hard X–ray emission from the HXT LO–channel during the time of the microwave maxima. The 86 GHz emission is double peaked with the first maximum coincident with the 14 GHz peak, and a second peak ∼15 seconds later.

The time evolution of flare images at the different wavelengths are shown in Figure 2. The soft X–ray snapshots, depicted in the leftmost column of Figure 2, show the flare as a single compact source ($\sim 8''$), plus emission from extended features. The gray scale of the SXT images is logarithmic, and therefore the actual soft X–ray flux from the extended loops is negligible when compared to the main source. Due to the low count rates in the HXT channels, the LO–channel hard X–ray maps, presented in the middle column of Figure 2, needed 40 seconds integration time. The count rates in the M1–channel were too low to produce a map. The maps from the LO–channel show a single unresolved source (the HXT maps have a spatial resolution of $5''$) at the same position as the soft X–ray source. Finally, the rightmost column of Figure 2 displays the millimeter maps from BIMA.

2.1. Millimeter emission

The millimeter maps, integrated over one minute, show a slightly extended source at the same site as the soft X–ray flare. The synthesized beam (i.e the instrumental response to a point source) is plotted at the bottom left corner of each of the millimeter maps on Figure 2. Since the flare occurred close to midday in California, the synthesized beam is quite small ($\sim 9'' \times 7''$). This is the highest spatial resolution achieved so far for a solar flare at millimeter wavelengths.

The physical parameters of the millimeter source (i.e., size and total flux density) were estimated by fitting the visibilities with a circular

Gaussian. The fit yields a source radius of 3-5″ throughout the flare. Once the source size has been determined, the brightness temperature, T_b, can be estimated using the Rayleigh Jeans approximation to the radio emission. The maximum brightness temperature calculated using the brightest pixel in the source ranges from $3-4\times10^5$ K. The optical depth is given by $T_b = T_e(1-e^{-\tau})$, where the electron temperature, T_e, obtained from the soft X–ray data (discussed in Section 3.3), is $10-15\times 10^6$ K. The resulting optical depth at 86 GHz is approximately 0.03-0.04, which confirms that the millimeter emission is indeed optically thin.

3. Results

In this section we first study the impulsive peak due to nonthermal emission which was observed at millimeter, microwave, and hard X–ray wavelengths. The radio spectrum composed of the microwave and millimeter emission is fitted by gyrosynchrotron radiation, and its fit parameters are discussed. Next, information obtained from the radio and hard X–ray spectra are used to determine the energy distribution of the accelerated electrons responsible for the impulsive nonthermal emission of this flare. Last, we discuss the emission during the gradual phase observed at millimeter and soft X–ray wavelengths.

3.1. Nonthermal emission

On 1994 August 18, the solar dedicated array at OVRO collected data at 45 frequencies from 1 to 18 GHz with 12 seconds temporal resolution. As mentioned earlier, due to a problem in determining the delay centers for the interferometer, and because the baselines of the small antennas have very low sensitivity, they cannot be calibrated. Thus, unfortunately, no imaging of the microwave emission is possible. Nevertheless, the total–power and the correlated data from the two large dishes (baseline 12) are available. The fringe spacing of baseline 12 is $46\farcm5/\nu$, for example at 5 GHz, with 30″ fringe spacing, emission from sources $\gtrsim 10''$are 'resolved out'. Since the millimeter emission is included in the spectral analysis, the correlated data (from a two element interferometer) rather than the total–power measurements are used to exclude emission from possible extended sources.

In order to study the radio spectrum during the impulsive peak, we combine the microwave and millimeter emission into the same spectrum. The thermal emission at microwave frequencies is negligible during the impulsive phase, whereas this is not true at millimeter wavelengths. The millimeter emission at 86 GHz is dominated by the thermal emission, even during the impulsive phase of this flare. Urpo et al. (1994) found a similar result for emission at 22 and 37 GHz. The authors report that for flares with peak intensity over 100 sfu at 22 GHz, the thermal bremsstrahlung is more important than the gyrosynchrotron emission. Thus, the thermal contribution at millimeter wavelengths has to be subtracted before the radio spectrum is constructed. We modeled the thermal contribution at 86 GHz with the same time profile as the soft X–ray emission (shown as a dotted line in Figure 3a). This thermal contribution is then subtracted from the 86 GHz flux density (solid line in Figure 3a). Figure 3b shows the resultant nonthermal millimeter flux density along with the emission at microwave frequencies.

Radio spectra from 1 to 86 GHz are shown in Figure 4 as stars. The microwave spectra in Figure 4 exhibits a dip in flux density at around 3–4 GHz. This sudden decrease in flux density is believed to be due to two sources which interfere destructively with each other (Fomalont and Wright 1974). The main source peaks at high frequencies (8-10 GHz), whereas the secondary source spectrum has a maximum at $\lesssim 2$ GHz. For the remainder of this discussion we concentrate on the high frequency source only, since it is the source most likely associated with the millimeter emission.

An unique feature of this flare is its composite high resolution microwave spectrum plus the 86 GHz data point during the impulsive phase. Early on, the high frequency spectral shape seen in Figure 4 resembles that of gyrosynchrotron emission, while after 2048 UT it is very flat from 5 to 14 GHz. Thus, before 2047 UT, the emission is caused by nonthermal electrons interacting with the magnetic field (nonthermal gyrosynchrotron), and after 2048 UT by thermal bremsstrahlung from the hot plasma (bottom right panel of Figure 4).

The physical parameters of the nonthermal electron population that produces the radio emission were determined by fitting the microwave plus millimeter spectrum as gyrosynchrotron radiation. Because of the high ambient density of $\sim 10^{11}$ cm^{-3} inferred from SXT images, the Razin suppression of radiation (Ramaty 1968, Ginzburg and Syrovatskii 1965) cannot be neglected. The gyrosynchrotron modeling was performed using the code described in Ramaty (1969) and Ramaty et al. (1994). From a fit to the observed spectrum, the total number of electrons, the power–law index of the electron energy spectrum, source size, and magnetic field can be estimated. In order to decrease the number of free parameters to be fitted, we assumed a constant magnetic field strength throughout the flare. We would like to point out that the radio spectrum cannot be fitted by an electron population with the same power–law index obtained from the hard X–ray spectrum ($\delta_x \sim 5 - 8$), which is too steep.

The adopted constant magnetic field strength was 250 Gauss. The photospheric magnetic fields determined from a Kitt Peak magnetogram taken the day before measured $\lesssim 300$ Gauss. However, since this flare occurred not far from the limb, the actual magnetic field strengths may be a factor of two larger than its line–of–sight value. As for the angle, θ, between the magnetic field and the line of sight, we chose $\theta = 66^o$ (the heliocentric longitude of the flare) which assumes radial magnetic field lines. The gyrosynchtroton fit with the Razin suppression taken into account is shown as a solid line in Figure 4. The following parameters were determined from the fit: δ_r, the power–law slope of the nonthermal electrons that produce the radio emission, the total number of energetic electrons, $N_e(E > E_0)$, and the nonthermal source radius.

The parameters of the nonthermal spectrum obtained for a constant magnetic field of 250 Gauss and $\theta = 66^o$ are shown in Figure 5. The total number of electrons above an energy cutoff ($E_0 = 10$ keV) determined from the fit is shown in Figure 5a. The spectral slope, δ_r of the nonthermal electrons that produced the radio emission is related to the high frequency slope, α, of the radio spectrum, by $\alpha = 0.90\delta_r - 1.22$, where the high frequency slope, α of the radio spectrum is well determined by the millimeter point at 86 GHz. The power–law index of the electron distribution so calculated ranges from 3.5–4.5 (triangles in Figure 5b). Also plotted on Figure 5b as stars is the electron energy slope inferred from the hard X–ray spectrum. Note that the discrepancy between the hard X–ray and radio power–law slopes is largest at the time of millimeter peak emission, this is so because both indexes seem to follow the soft–hard–soft behavior with respect to their light curves. The index from the hard X–rays is hardest at the time of peak hard X–rays (2045:30 UT), whereas the radio index reaches its lowest value at 2046:30 UT, the time of the second millimeter peak.

The steady source size increase may be due to a real expansion of the source in response to the energy input or may be caused by the activation of neighboring magnetic flux tubes. The model suggest that the nonthermal radio source is small, $<5''$ at first(Figure 5c), and then increases steadily to $15''$at 2047:30 UT. We would like to point out that the flaring loop seen in SXT images if very compact ($\lesssim 8''$) and the hard X–ray source is unresolved in HXT images. Such a small source cannot be resolved by OVRO or BIMA. Time profiles of the emission at different wavelengths are shown on Figure 5d for reference.

3.2. Electron energy distribution

The energy distribution of the nonthermal electrons is obtained by combining the hard X–ray and radio spectral information. The hard X–ray emission (<33 keV) detected by HXT originate from lower energy electrons ($\lesssim$ 50keV), whereas the microwaves are produced by few hundred keV electrons, and the millimeter emission from $\gtrsim$ 0.5 MeV electrons (White and Kundu 1992, Kundu et al. 1994). The three panels of Figure 6 show the electron energy spectrum (for $E_0 = 10$ keV) constructed from the hard X–ray and radio spectra at the time of peak of hard X–ray (2045:27 UT), microwave (2045:51 UT), and millimeter (2046:39 UT) emissions. Electrons in the 20-50 keV energy range are assumed to produce the hard X–ray (dashed line in Figure 6), while the microwave/millimeter emission is thought to originate from $\gtrsim$ 300 keV electrons (solid line). The electron density spectrum is clearly not a single power–law, but a double power–law that flattens at $\sim$ 30-50 keV energies. The energy at which the spectrum breaks up, that is where the slope changes from δ_x to δ_r for higher energies ranges from $\sim$ 55 keV at 2045:27 UT and then decreases to $\sim$ 30 keV at 2047 UT.

The temporal evolution of the accelerated electrons determined from the synthetic spectra shown in Figure 6 is shown for several low energy cutoffs in Figure 7. As can be seen from this figure, the lower energy (<50 keV) electrons are accelerated earlier, prior to 2046 UT, whereas the higher energy (>100 keV) electrons are progressively accelerated later. The number of mid energy range (100-200 keV) electrons peak at 2046 UT, whereas the MeV electrons are more abundant 20 minutes later. This type of energy distribution suggests that the high energy electrons were accelerated later on, implying that more time (half a minute) is needed to accelerate electrons up to high (>500 keV) energies.

3.3. Thermal emission

Temperature and emission measure maps were made from ratios of different SXT filter images (Vaiana et al. 1973, Gerassimenko and Nolte 1978, McTiernan et al. 1993). The average temperature and total emission measure of the soft X–ray source as function of time were determined for a region 3×3 pixels around the main source centroid (1 pixel = $2\rlap{.}''455$). Since the values of temperature and emission measure are used in the computation of the predicted radio flux, we chose such a small region to guarantee that this flux density would not be "resolved out" by the BIMA interferometer. Early on $T_e \sim 14$ MK, the electron temperature then decreases monotonically to $\sim$ 10 Mk at 2052

UT; the emission measure increases from 10^{48} cm^{-3} to its peak value of 3.4×10^{48} cm^{-3} at 2047:40 UT and then returns to its initial 10^{48} cm^{-3} level. Once the temperature and emission measure are known, the free–free flux density that such a source would produce at 86 GHz is calculated (White and Kundu 1992).

Plotted on Figure 8 are the flux density from BIMA's shortest baseline (solid line) and the predicted free-free emission from the soft X–rays from SXT (stars) and GOES (dashed line). Since GOES detects emission from the entire sun, the free–free flux calculated from its emission is that of the entire solar disk and, therefore, is not expected to agree with the observed flux density from BIMA which "resolves out" flux from extended sources. The predicted flux density is a lower limit of the total free–free flux density, since only a small region was considered. Millimeter emission prior to 2047 UT is likely nonthermal, and thus should not be compared to the free–free emission. Only after the peak of the gradual phase at 2049 UT is there good agreement between the observed and predicted thermal emission. We would like to point out that a source of uncertainty in the computation of the radio flux predicted from the soft X–rays relies on the uncertainties of solar abundances of metals. Since the soft X–rays from $10^6 - 10^7$ K plasma are mainly in X–ray lines in the filters used, the soft X–ray data primarily measure the emission measure of heavier elements. In order to determine the emission measure of hydrogen (which is responsible for the radio emission), we have assumed solar coronal abundances.

Even for such a small region, the predicted flux density from the SXT source is higher by about 20% than that observed. An explanation for such a discrepancy may be that the source at this time is not isothermal. A multi–temperature source was required to resolve the discrepancy between the observed millimeter flux density and the predicted optically thin emission from the soft X–ray thermal plasma, for a flare that occurred the day before (Silva et al. 1996).

4. Discussion and Conclusions

The flare on 18 August 1994, which occurred in active region AR 7765, consisted of a single compact source ($\lesssim 8''$) in size, seen in SXT, HXT LO–channel, and millimeter maps. Thus, this is the first flare for which the source of millimeter emission is shown to coincide in space with the emission observed at other wavelengths, thereby supporting its association with observations at other wavelengths. Even though it is not possible to map the microwave emission from OVRO for this period, the single correlated baseline observations hint at the presence of two sources. The high frequency source is likely to be the source seen in the hard X–ray and millimeter maps during the impulsive phase because of the similarity between the time profiles of the 10-15 GHz and the 86 GHz emissions. The millimeter maps of this flare show that both impulsive and gradual emissions at 86 GHz originated from the same source shown in Figure 2. This is probably due to the compactedness of the loop which precludes it from being resolved into a footpoint and loop top sources.

The most important feature of this flare is the impulsive peak at ~2046:30 UT observed by BIMA. The early (2045:30-2047:30 UT) radio spectrum is constructed from the OVRO microwave data (2 to 15 GHz) plus the millimeter flux density at 86 GHz with its thermal contribution subtracted. The radio spectrum is well fitted by nonthermal gyrosynchrotron radiation from power–law electrons with Razin suppression (Ramaty 1969) taken into account. The millimeter point at 86 GHz is crucial in determining the high frequency slope of the nonthermal radio spectrum and thereby obtaining the power–law index, δ_r, of the nonthermal electrons responsible for the radio emission. The nonthermal electrons that created the radio emission do not appear to follow the same power–law as inferred for the electrons responsible for the hard X–rays, implying that the energy spectrum of the nonthermal electrons accelerated in this flare follows a double power–law. That is, the electron energy spectrum has a power–law slope of $\sim 6-8$ below ~ 40 keV, and becomes harder with a slope of ~ 4 for energies higher than this break energy. The double power–law energy spectrum result is not what is commonly found when comparing the slope of microwave spectra with that of the hard X–ray spectra, which are usually found to be approximately equal (Wang et al. 1994).

Noteworthy is that these small flares with double power–law electron spectra may be the result of a detection bias. That is, had the radio emission been produced by electrons with steep power-law indexes as δ_x, such flares would not have been detected at millimeter wavelengths because the flux densities would be below the detection threshold of BIMA. Conversely, if the hard X–ray spectrum was as hard as that implied from the radio observations, the hard X–rays would not have been detected either.

Previous comparisons of hard X–rays and microwave spectra have also implied break ups in the electron energy distribution. Bai and Ramaty (1976) inferred a break in the spectrum around 0.8 MeV. Kundu et al. (1994) inferred a double power–law spectrum for the accelerated electrons with $\delta_x \sim 7-9$ and $\delta_r \sim 2.5-6$ for 8 small to average size flares.

Such a spectral hardening was also observed in hard X–ray/γ–ray spectra of large flares observed by the Solar Maximum Mission during the maximum of the previous solar cycle (Dennis 1988, Smith and Orwig 1988, Vestrand 1988). It is interesting to note that the same acceleration mechanism is at work in these small flares and that such small flares accelerate electrons up to MeV energies. These high energy electrons from small flares can only be inferred from radio observations, since the small number of gamma–ray photons produced in such small flares are below the detection threshold of current hard X–ray detectors.

The temporal evolution of the electron density at different low energy cutoffs calculated for this flare has shown that higher energy electrons were progressively accelerated later supporting the two phases acceleration model (Wild et al. 1963, de Jager 1969). This result reflects the rather large time delays of about 30 s between the maxima of emission at different wavelengths. Thus, the second acceleration mechanism in this flare took 30 s to accelerate electrons to higher energies and created a high energy component with a significantly flatter spectrum. Current suggestions for the observed spectral hardening involve further acceleration of low energy electrons into higher energy ones, for example by plasma wave–particle interactions (Winglee et al. 1991) or second step Fermi acceleration. An alternative explanation is that the broken power–law may be the result of an anisotropic acceleration mechanism. In this scenario, the enhancement of high energy electrons may be an indication of a preferential acceleration perpendicular to the magnetic field since the radio emission is produced by electrons with perpendicular velocity components, whereas the hard X–rays are produced isotropically with respect to the magnetic field direction by collisions.

A comparison of the predicted free–free radio flux density from the soft X–ray source yields a good match with the millimeter flux density after 2049 UT. The disagreement between the two flux densities at around 2048 UT, cannot be accounted for by the BIMA interferometer 'resolving out' part of the flux, but may be explained if the source is not isothermal.

Acknowledgements

We would like to thank W. J. Welch, the director of BIMA, for allowing a flexible observing schedule (dependent on solar activity). We are grateful to J. M. McTiernan for providing the *Yohkoh* data. AVRS acknowledges support by NSF grant AST 93-20238. Solar radiophysics at the University of Maryland is supported by NSF grant ATM 93-16972, by NASA grant NAG W-1541, and NASA/CGRO grant NAG 5-1450. The use of BIMA for scientific research is supported by NSF grant AST 93-14847.

References

Bai, T. and Ramaty, R.: 1976, *Solar Phys.*, **49**, 343.

de Jager, C.: 1969, in C. de Jager and Z. Svetska (eds.), *Cospar Symposium on Solar Flares and Space Research*, p. 1.

Dennis, B. R.: 1988, *Solar Phys.*, **118**, 49.

Dulk, G. A.: 1985, *Ann. Rev. Astron. Astrophs.*, **23**, 169.

Fomalont, E. B. and Wright, M. C. H.: 1974, "Interferometry and Aperture Synthesis" in *Galactic and Extragalactic Radio Astronomy*, ed. by G. L. Verschuur, K. I. Kellermann (Springer, New York, Heidelberg, Berlin), p. 256.

Frost, K. J. and Dennis, B. R.: 1971, *Astrophys. J.*, **165**, 655.

Gary, D. E. and Hurford, G. J.: 1990, *Astrophys. J.*, **361**, 290.

Gerassimenko, M. and Nolte, J. T.: 1978, *Solar Phys.* **60**, 299.

Ginzburg, V. L. and Syrovatskii, S. I.: 1965, *Ann. Rev. Astron. Astrophs.*, **3**, 297.

Kosugi, T., Makishima, K., Murakami, T., Sakao, T., Dotani, T., Inda, M., Kai, K., Masuda, S., Nakajima, H., Ogawara, Y., Sawa, M., and Shibasaki, K.: 1991, *Solar Phys.*, **136**, 17.

Kundu, M. R., White, S. M., Gopalswamy, N., Bieging, J. H., and Hurford, G. J.: 1990, *Astrophys. J.-Letters*, **358**, L69.

Kundu, M. R., White, S. M., Gopalswamy, and Lim, J.: 1994, *Astrophys. J. Suppl. Ser.*, **90**, 599.

Lim, J., White, S. M., Kundu, M. R., and Gary, D. E.:1992, *Solar Phys.*, **140**, 343.

McTiernan, J. M., Kane, S.R., Loran, J. M., Lemen, J. R., Acton, L. W., Hara, H., Tsuneta, S., and Kosugi, T.: 1993, *Astrophys. J.-Letters*, **416**, L91.

Ramaty, R.: 1968, *J. G. R.*, **73**, 3573.

Ramaty, R.: 1969, *Astrophys. J.*, **158**, 753.

Ramaty, R. and Petrosian, V.: 1972, *Astrophys. J.*, **178**, 241.

Ramaty, R., Schwartz, R. A., Enome, S. and Nakajima, H.: 1994, *Astrophys. J.*, **436**, 941.

Silva, A. V. R., White, S. M., Lin, R. P., de Pater, I., Shibasaki, K., Hudson, H. S., and Kundu, M. R.: 1996, *Astrophys. J.-Letters*, **458**, L49.

Smith, D. F. and Orwig, L. E.: 1988, *Astrophys. J.*, **327**, 466.

Tsuneta, S., Acton, L., Bruner, M., Lemen, J., Brown, W., Carvalho, R., Cortura, R., Freeland, S., Jurcevich, B., Morrison, M., Ogawara, Y., Hirayama, T., and Owens, J.: 1991, *Solar Phys.*, **136**, 37.

Urpo, S., Bakhareva, N. M., Zaitsev, V. V., and Stepanov, A. V.: 1994, *Solar Phys.*, **154**, 317.

Vaiana, G. S., Krieger, A. S., and Timothy, A. F.: 1973, *Solar Phys.*, **32**, 81.

Vestrand, W. T.: 1988, *Solar Phys.*, **118**, 95.

Wang, H., Gary, D. E., Lim, J., and Schwartz, R. A.: 1994, *Astrophys. J.*, **433**, 379.

White, S. M. and Kundu, M. R.: 1992, *Solar Phys.*, **141**, 347.

Wild, J. P., Smerd, S. F., and Weiss, A. A.: 1963, *Ann. Rev. Astron. Astrophys.*, **1**, 291.

Winglee, R. M., Kiplinger, A. L., Zarro, D. M., Dulk, G. A., and Lemen, J. R.: 1991, *Astrophys. J.*, **375**, 366.

Wright, M. C. H. and Sault, R. J.: 1993, *Astrophys. J.*, **402**, 546.

Figure 1. **Top:** The soft (crosses) and hard X–ray emission from SXT and HXT LO (solid line) and M1–channel (dotted line) for the 18 August 1994 flare. **Bottom:** Radio emission from the flare, the millimeter emission from BIMA is plotted as a solid line, while the 5 GHz and the 14 GHz from OVRO are plotted as dotted and dashed lines, respectively. The millimeter flux density follows the scale on the right hand side of the plot.

Figure 2. SXT snapshots, HXT LO–channel maps (40 seconds integration), and millimeter maps (1 minute integration) at 86 GHz of the flare are shown on the leftmost, middle and rightmost column, respectively. The time of each image is displayed at the bottom of it. The BIMA beam is shown at the bottom left corner of each millimeter map. The millimeter source contours are 5, 10, 20, 40, 60, 80, and 99% of 0.61 sfu (the peak value of the millimeter maps). The vertical streaks in the two earlier SXT images are due to pixel saturation.

Figure 3. Time profiles of **a)** the millimeter evolution with the thermal component model (dotted line), and **b)** the millimeter emission (solid line) after the thermal component has been subtracted. Also plotted are the 5 (dotted line) and 14 GHz (dashed line) flux densities.

Figure 4. Plots of the radio spectrum from the observed microwave and millimeter flux density (stars) at the peak of hard X–ray (2045:39 UT), microwave (2046:15 UT), and millimeter(2046:39 UT) emissions, plus a spectrum late in the flare (2049 UT) after the soft X–ray maxima. The solid line represents nonthermal gyrosynchrotron emission (with Razin suppression taken into account) from a model with constant magnetic field strength, whereas the thermal bremsstrahlung is plotted as a dashed line in the last panel. Only the high frequency source is modeled.

Figure 5. The parameters obtained from a gyrosynchrotron model with fixed magnetic field of 250 Gauss and $\theta = 66^o$. **a)** Total number of electrons, $N_e(E > 10$ keV), **b)** power–law index of the electron energy spectrum determined from the radio (crosses) and hard X–ray (stars), **c)** area of the nonthermal source, and **d)** temporal evolution at various wavelengths: 86 (solid), 14 (dotted) and 5 GHz (dashed).

Figure 6. Differential energy spectrum of the electrons calculated from the hard X–ray (dashed line) and microwave/millimeter (solid line) spectra at the time of the hard X–ray, microwave, and millimeter peaks.

Figure 7. Temporal evolution of the total number of electrons, above a certain energy cutoff (E_o) labeled for each curve, calculated from the synthetic energy spectra shown in the previous figure. Curves with E_o <50 keV were obtained from the hard X–ray flux, whereas those with E_o >100 keV are from the radio spectra.

Figure 8. The free–free radio flux density predicted from the temperature and emission measure of soft X–ray emission calculated from a small region of the *Yohkoh* SXT source (stars) and from GOES soft X–ray flux (dashed line) from the whole sun. The observed millimeter flux density (solid line) is also plotted for comparison.

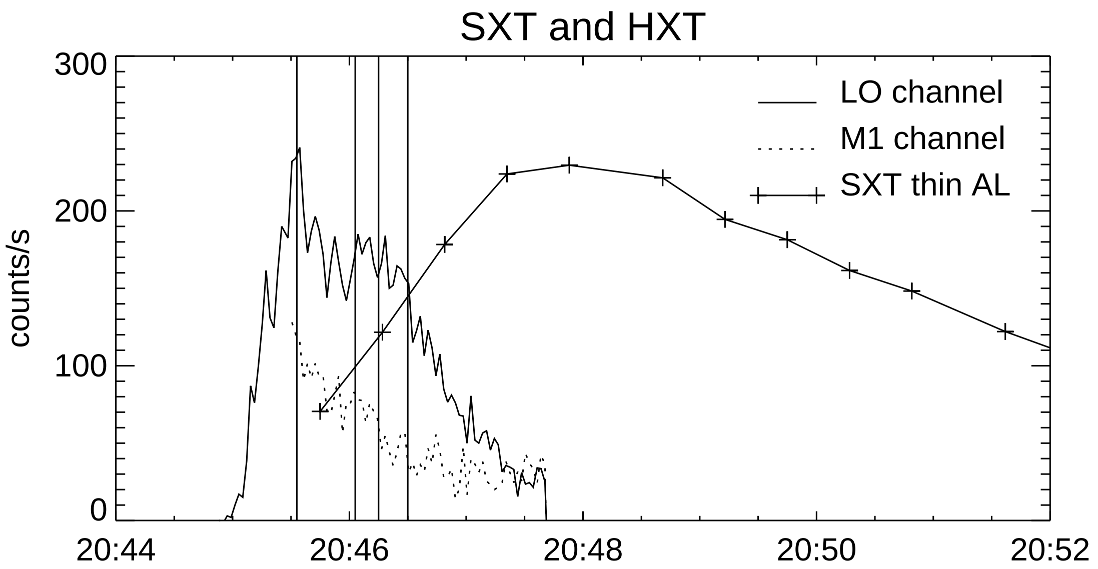

SXT and HXT
300
200
100
0
counts/s
LO channel
M1 channel
SXT thin AL
20:44
20:46
20:48
20:50
20:52

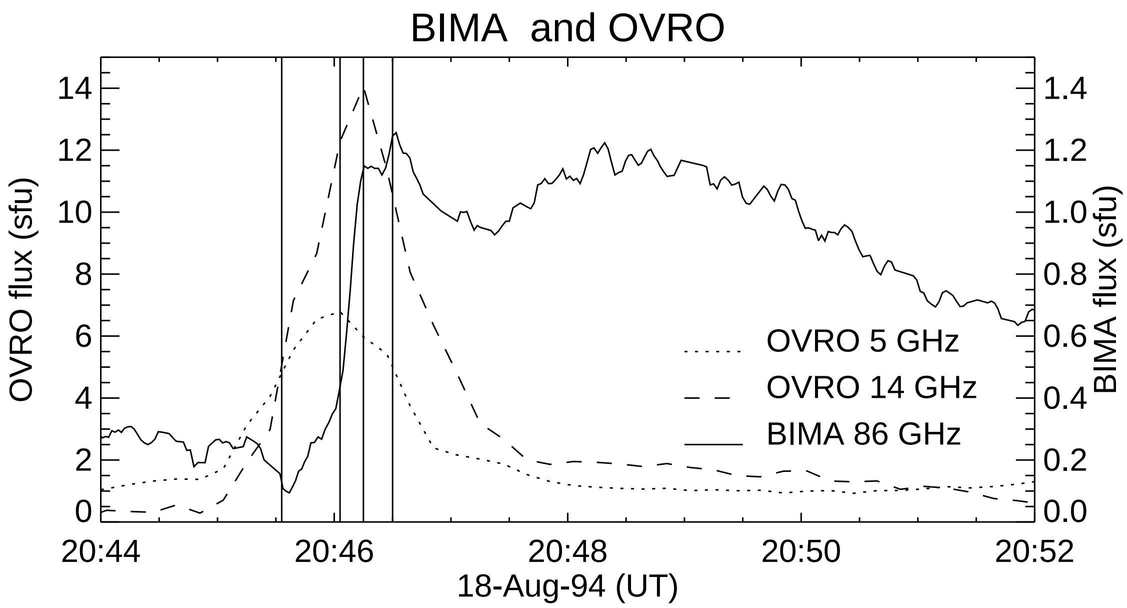

BIMA and OVRO
14
12
10
8
6
4
2
0
OVRO flux (sfu)
1.4
1.2
1.0
0.8
0.6
0.4
0.2
0.0
BIMA flux (sfu)
OVRO 5 GHz
OVRO 14 GHz
BIMA 86 GHz
20:44
20:46
20:48
20:50
20:52
18-Aug-94 (UT)

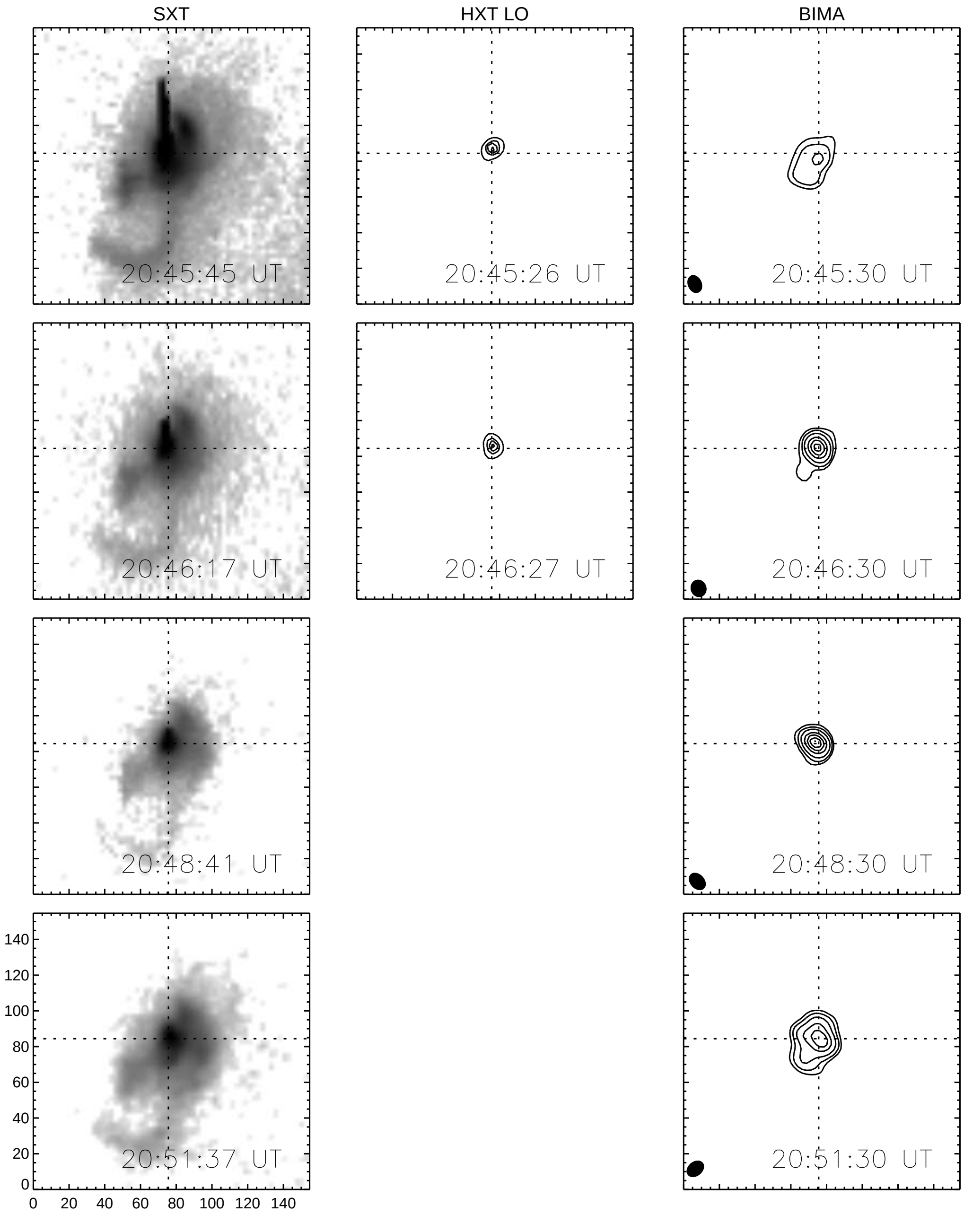

SXT
HXT LO
BIMA
20:45:45 UT
20:45:26 UT
20:45:30 UT
20:46:17 UT
20:46:27 UT
20:46:30 UT
20:48:41 UT
20:48:30 UT
20:51:37 UT
20:51:30 UT
0
20
40
60
80
100
120
140

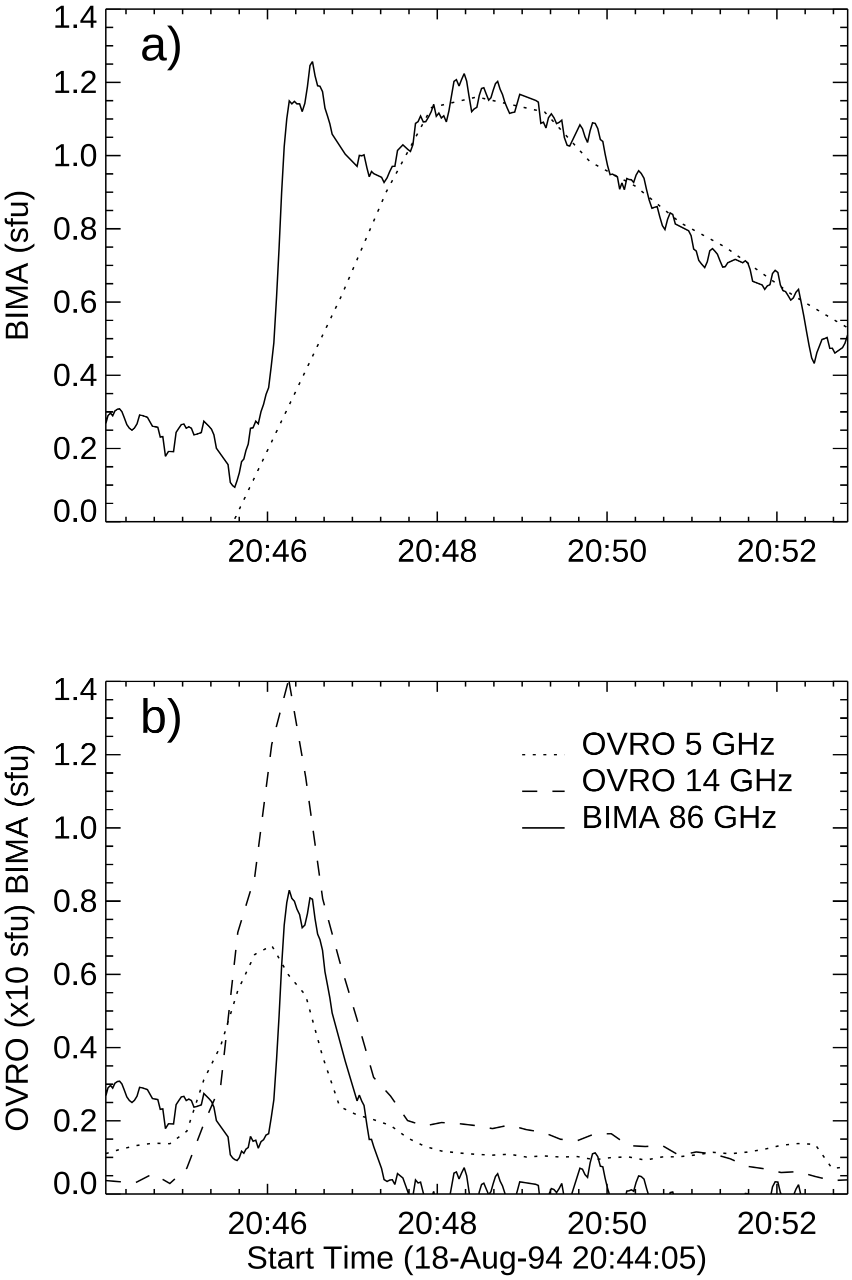

a)
BIMA (sfu)
1.4
1.2
1.0
0.8
0.6
0.4
0.2
0.0
20:46
20:48
20:50
20:52
b)
OVRO (x10 sfu) BIMA (sfu)
OVRO 5 GHz
OVRO 14 GHz
BIMA 86 GHz
Start Time (18-Aug-94 20:44:05)

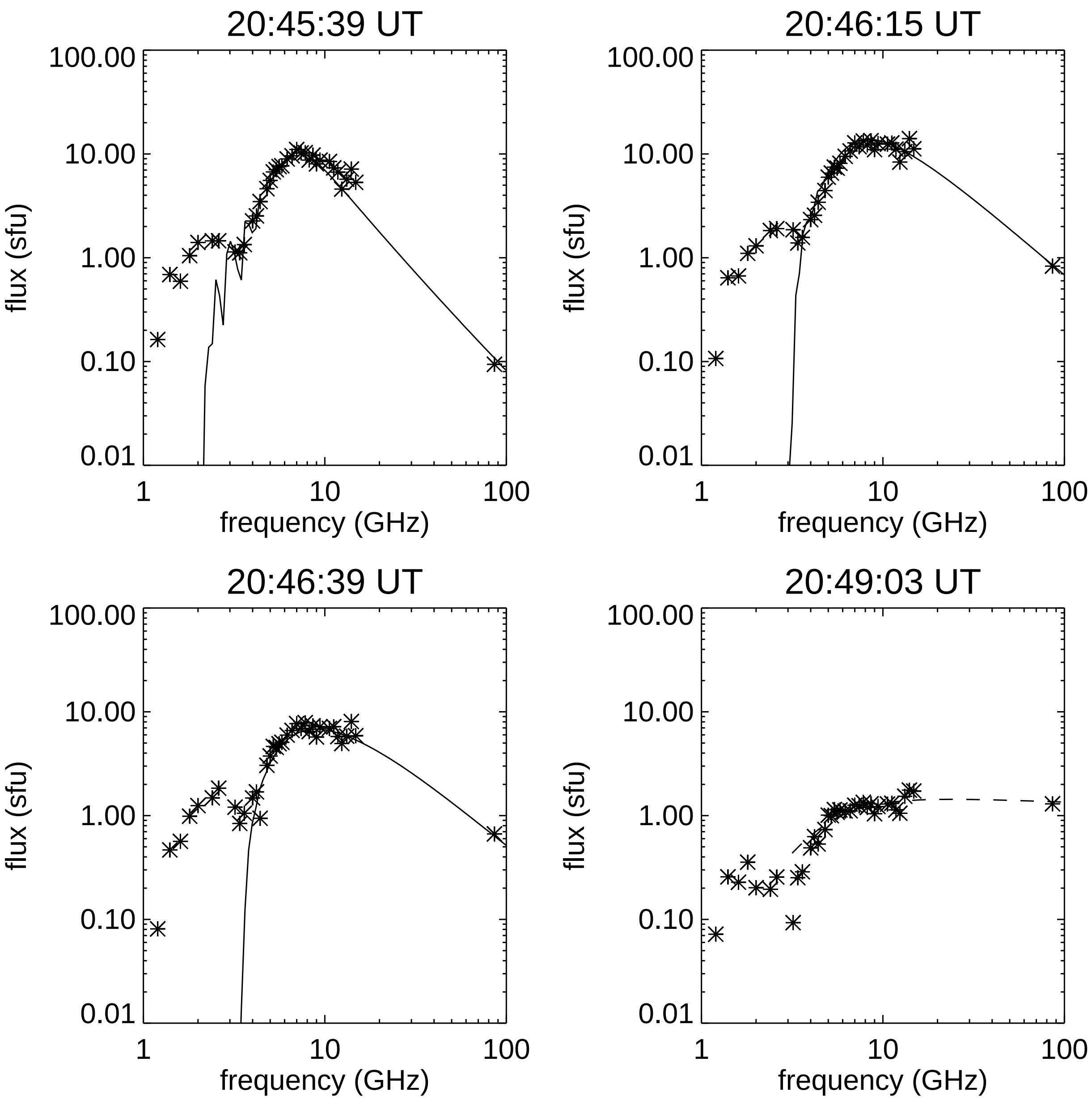
20:45:39 UT
20:46:15 UT
20:46:39 UT
20:49:03 UT
flux (sfu)
frequency (GHz)
100.00
10.00
1.00
0.10
0.01
1
10
100

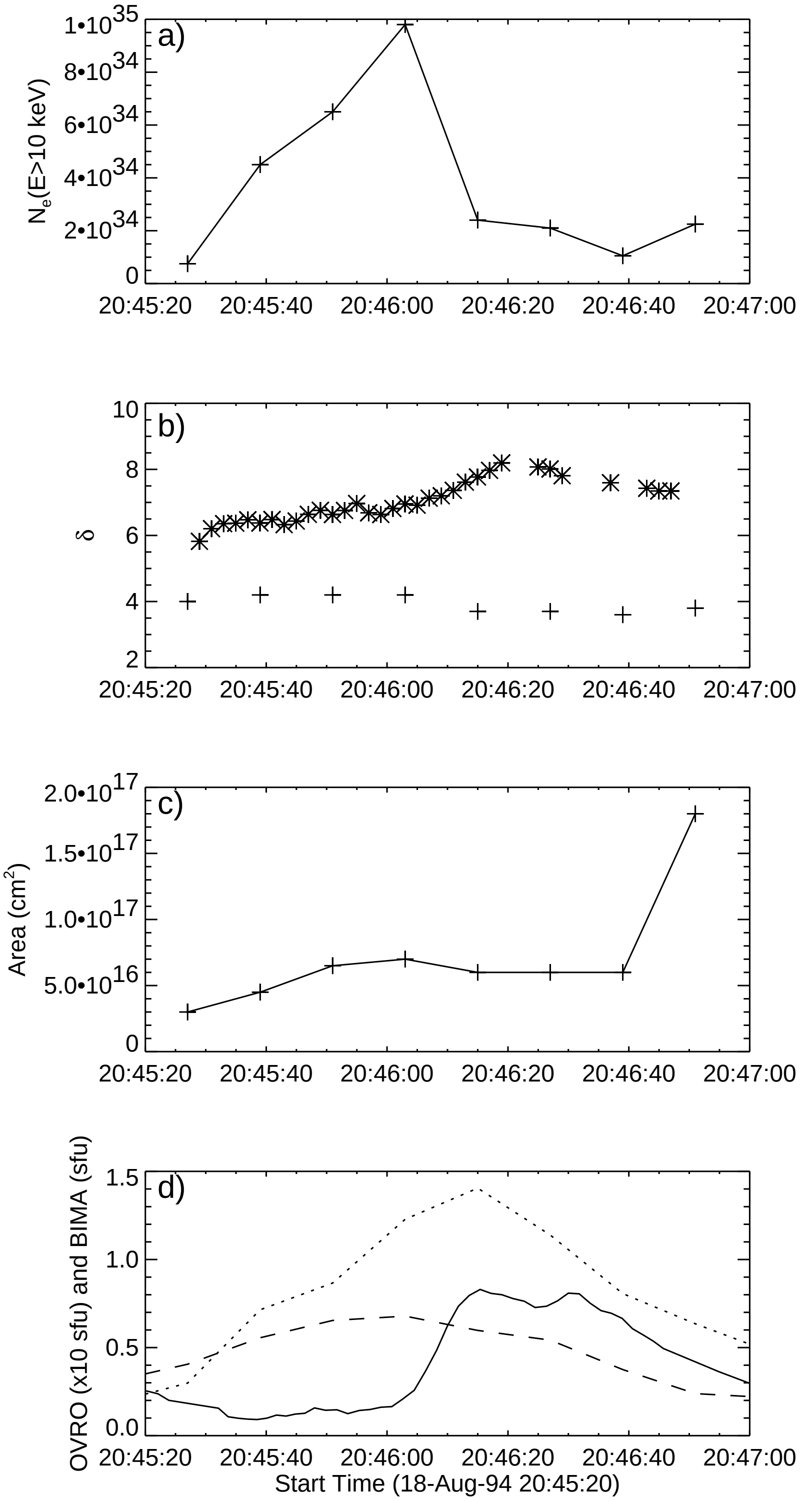

a)
N_e(E>10 keV)
$1•10^{35}$
$8•10^{34}$
$6•10^{34}$
$4•10^{34}$
$2•10^{34}$
0
20:45:20 20:45:40 20:46:00 20:46:20 20:46:40 20:47:00
b)
δ
10
8
6
4
2
20:45:20 20:45:40 20:46:00 20:46:20 20:46:40 20:47:00
c)
Area (cm^2)
$2.0•10^{17}$
$1.5•10^{17}$
$1.0•10^{17}$
$5.0•10^{16}$
0
20:45:20 20:45:40 20:46:00 20:46:20 20:46:40 20:47:00
d)
OVRO (x10 sfu) and BIMA (sfu)
1.5
1.0
0.5
0.0
20:45:20 20:45:40 20:46:00 20:46:20 20:46:40 20:47:00
Start Time (18-Aug-94 20:45:20)

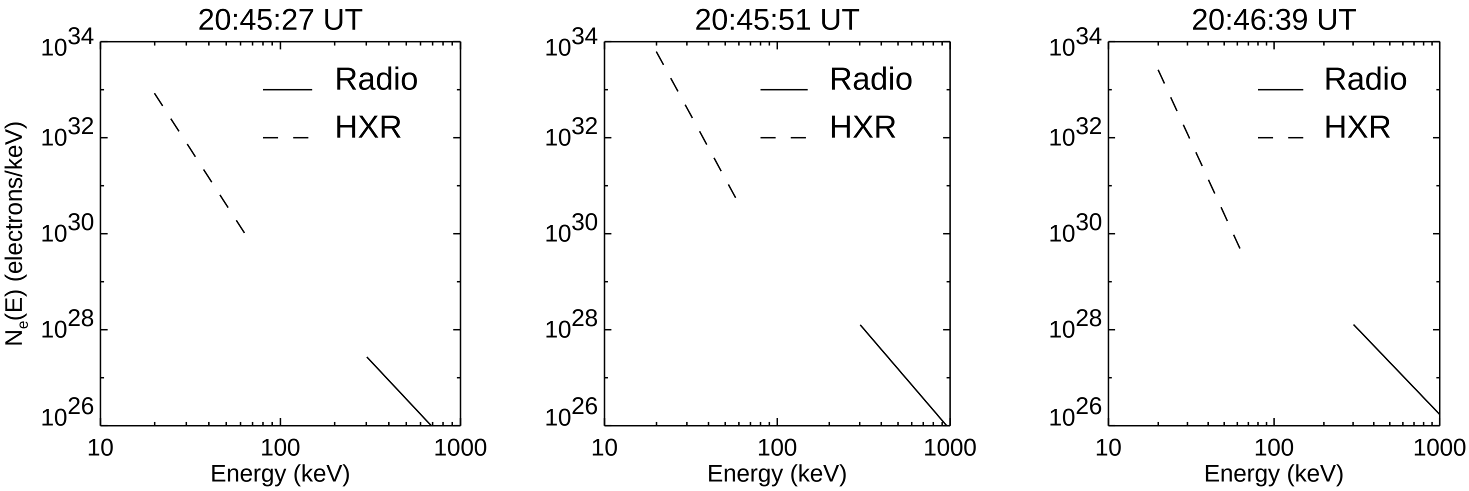

20:45:27 UT
20:45:51 UT
20:46:39 UT
Radio
HXR
$N_e(E)$ (electrons/keV)
10^{26}
10^{28}
10^{30}
10^{32}
10^{34}
10
100
1000
Energy (keV)

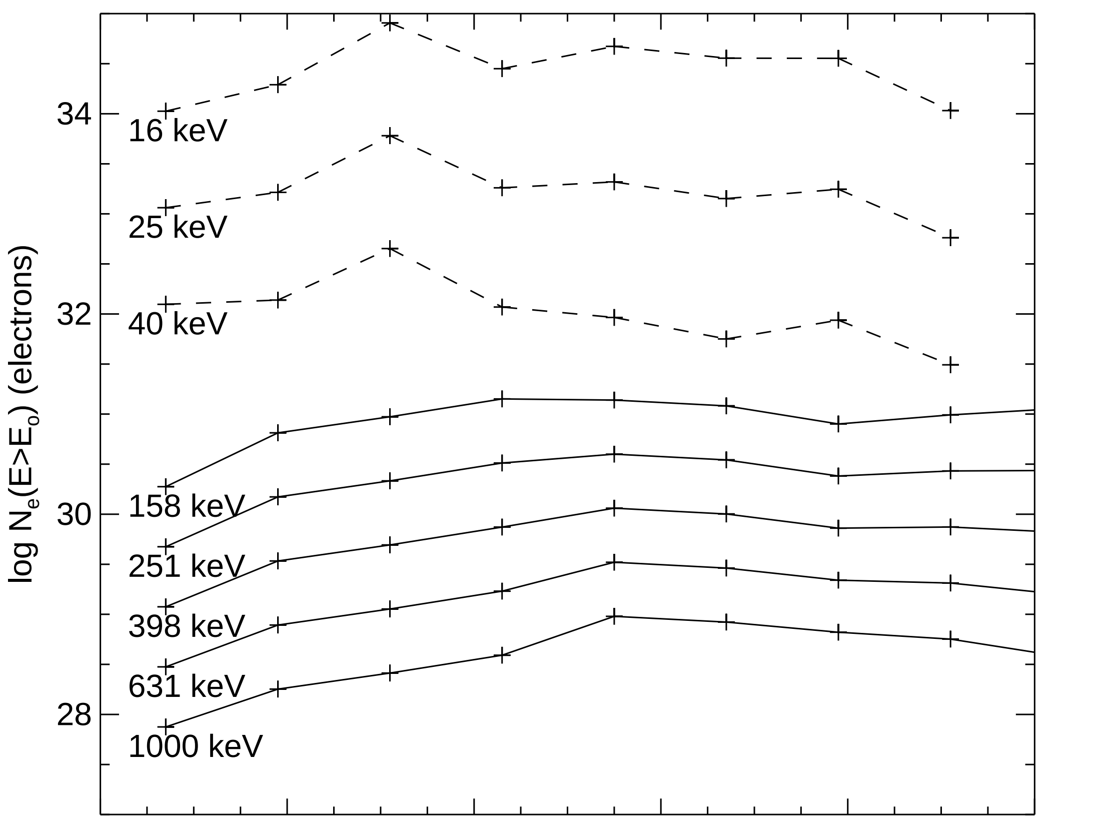

34
32
30
28
16 keV
25 keV
40 keV
158 keV
251 keV
398 keV
631 keV
1000 keV
log $N_e(E>E_o)$ (electrons)
20:45:20
20:45:40
20:46:00
20:46:20
20:46:40
20:47:00
Start Time (18-Aug-94 20:45:20)

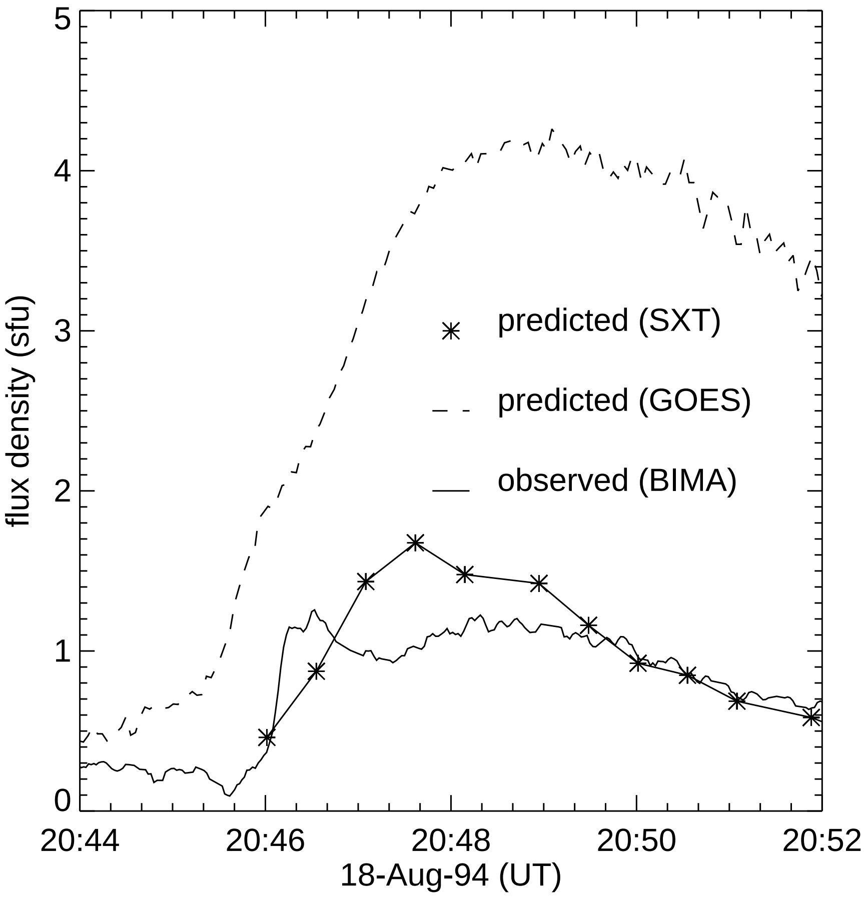

5
4
3
2
1
0
flux density (sfu)
predicted (SXT)
predicted (GOES)
observed (BIMA)
20:44
20:46
20:48
20:50
20:52
18-Aug-94 (UT)